Intent Modeling and Conflict Probability Calculation for Operations in Upper Class E Airspace

Min Xue* Jaewoo Jung† Jeffrey Homola‡
NASA Ames Research Center, Moffett Field, CA 94035

This work presents a probabilistic operational intent model for vehicles operating in upper Class E airspace. A hybrid method is developed to calculate the intent conflict probability leveraging and extending past works on probabilistic conflict computation. Simulation results verify that the probabilistic intent model can accurately encompass the uncertain positions of each vehicle type, that are a result of wind prediction errors and vehicle performance. A comparison with past methods showed that the proposed hybrid method captures the intent conflict probability with better accuracy, especially for a larger look-ahead horizon, and computational time is reasonable for real-time applications. An example is presented to illustrate the use of the intent conflict probability in strategic planning applications.

I. Introduction

The technology development of balloons [1], airships [2], and high-altitude long-endurance (HALE) high-aspect-ratio wing aerial vehicles [3, 4] has expedited the deployment of high altitude operations above Flight Level (FL) 600. It allows broader service area coverage than at ground level. To accommodate the increasing demand of commercial applications, the Federal Aviation Administration (FAA) published the first concept of operations for upper Class E Traffic Management (ETM) and proposed the concept of cooperative operations [5].

Several architectures [6–8] have been proposed recently for cooperative operations in ETM by leveraging principles from the Unmanned Aircraft System (UAS) Traffic Management (UTM) concept. The UTM system was developed by NASA in collaboration with the FAA and industry and has demonstrated the ability to support safe, efficient, and scalable operations of small UAS under 400 feet Above Ground Level (AGL) [9]. To support cooperative operations, a key assumption is that operational intent must be shared among operators. To that end, understanding and defining how to model operational intent is critical to the success of ETM, where a variety of vehicle performances are involved.

Early studies of flight intent can be traced back to the Free-Flight concept [10], where operators were envisioned to alter their flight plans in real time without prior approval of ground controllers. Zhao et al. [11] listed several forms of intent: motive intent, objective intent, trajectory intent, and cost intent, where the motive intent includes information of turn, climb/descent, and speed, and was categorized as the short-term intent. In Europe, Ruigrok et al. [12] defined the aircraft intent as the 4D path with four different look-ahead times. In these studies, flight intents are delivered in the form of flight plans, or Trajectory Change Points (TCPs), through an Automatic Dependent Surveillance - Broadcast (ADS-B) message. Intent inference algorithms [13, 14] were even developed to help obtain the predicted intent information in case such intent can not be acquired through ADS-B in time. Once the intent is acquired, it was then used for probabilistic aircraft trajectory/location prediction [14, 15] by including uncertainties. Therefore, in the Free-Flight concept, the flight intent and probabilistic aircraft trajectory/location prediction are two separate steps.

In the UTM concept [16], the flight intent of an operation is submitted and shared in the form of an operation plan. As stated in the UTM concept of operations, the operation plan should be developed prior to the operation and indicate the four-dimensional (4D) volume of airspace within which the operation is expected to occur. Furthermore, segmentation of the 4D volume is encouraged to promote the efficient use of airspace. According to this definition, the flight intent, or operational intent, in the UTM concept is distinguished from the flight plan (or the flight intent defined in the Free-Flight concept) as the operational intent refers to the resulting probabilistic aircraft trajectory/locations. This indicates that the operational intent in the UTM concept has a broader scope (including the trajectory prediction and the uncertainty prediction) than its counterpart in the Free-Flight concept. The broader scope of operational intent in UTM is possible due to the functionality of ground-based service suppliers in the UTM system. These service suppliers are empowered with adequate computational capability and complement the FAA-provided air traffic service, forming

*Aerospace Research Engineer, Aviation Systems Division. Mail Stop 210-15. AIAA senior member.
†Aerospace Research Engineer, Aviation Systems Division. Mail Stop 210-6. AIAA senior member.
‡Aerospace Research Engineer, Human System Integration Division. Mail Stop 262-4. AIAA member.

a network to share data and provide extra services, such as operational intent to support operations. To support the cooperative operation concept using a UTM-like construct, the definition of the broader scope of the flight intent is adopted in this work.

This work proposes a probabilistic operational intent model for vehicles in an ETM operational environment. Simulations have been conducted to verify the operational intent model. To compute the intent conflict probability, several approximated analytical methods [17, 18] were revisited, and a hybrid method was developed based on these methods to address the needs of strategic planning. An example is also presented to illustrate the usage of intent conflict probability in strategic planning.

The paper is organized as follows: Section II presents the probabilistic intent model for different vehicle types and demonstrates how simulation was used for verification of the model. Section III proposes a new hybrid method for calculating the probability of operational intent conflict and its comparison to previous methods. Section IV shows an illustrative example for strategic planning using the intent conflict probability, and Section V concludes this work.

II. Probabilistic Operational Intent Model

As discussed previously, the operational intent in this work includes probabilistic aircraft locations within a given time period resulting from the flight plan, flight performance, and wind prediction errors. In order to construct the probabilistic aircraft locations based on the flight plan, past works on probabilistic trajectory prediction were leveraged [17, 18]. If an aircraft can perfectly follow a flight plan and the wind prediction is accurate, the 4D locations of the aircraft at any time in the future will be deterministic, and the operational intent will precisely match the predicted reference trajectory. However, since there are always errors/uncertainty in wind prediction, navigation, tracking, and control, the aircraft location prediction becomes probabilistic and the operational intent size gets inflated.

Given a flight plan that provides a flight path (e.g., waypoints and true air speed) and flight modes (e.g., constant speed, constant turn, etc.), a simple linear hybrid system using predefined flight modes [18] can be used to estimate the nominal trajectory as in Eqn. 1, where $\hat{\vec{X}} = [\hat{\vec{x}}^T \ \hat{\vec{v}}^T]^T$ includes the estimated location $\hat{\vec{x}}$ and velocity $\hat{\vec{v}}$. $\hat{\vec{W}} = [0\,0\,0\ \hat{\vec{w}}^T]^T$ contains estimated wind speeds and R_e^h is the rotation matrix to convert the wind from the Earth frame to the frame that aligns with the aircraft heading.

$$\hat{\vec{X}}(t_i) = A\hat{\vec{X}}(t_{i-1}) + \begin{bmatrix} R_e^h & 0_{3\times3} \\ 0_{3\times3} & R_e^h \end{bmatrix} \hat{\vec{W}} \tag{1}$$

Assuming $\vec{x}$ denotes the actual aircraft location, the error $\tilde{\vec{x}}$ will then be:

$$\tilde{\vec{x}}(t_i) = \vec{x}(t_i) - \hat{\vec{x}}(t_i) \tag{2}$$

Assuming the position prediction error follows a zero-mean normal distribution with covariance Σ in the horizontal plane, the pdf of $\vec{x}$ at time t_i can be expressed as:

$$p[\vec{x}(t_i)] = \mathcal{N}(\vec{x}; \bar{\vec{x}}, \Sigma) \tag{3}$$

The errors of the aircraft location at a given time can be divided into three directions: along-track, cross-track, and vertical. Since aircraft, including airship and high-altitude long-endurance aircraft, are typically flown at a constant airspeed or Mach number, the prediction accuracy of aircraft position is largely affected by wind prediction errors. In terms of aircraft performance, two different situations are discussed in the following sections.

A. With adequate lateral control

For aircraft with adequate thrust and advanced control and navigation, the error in wind prediction mostly affects the along-track position prediction error, which grows with time. The cross-track and vertical errors are caused by the aircraft's performance in navigation, tracking, and control, and these errors are usually constant and time-independent. The error covariance matrix Σ in a frame that aligns with aircraft heading can then be expressed by Eqn. 4, where the σ_c and σ_h are stationary root mean square deviations in the cross-track and vertical directions. The σ_a is the growth rate of the root mean square deviation primarily determined by the wind speed prediction error along the track.

$$\Sigma(t_i) = \begin{bmatrix} \sigma_a^2(t_i - t_0)^2 & 0 & 0 \\ 0 & \sigma_c^2 & 0 \\ 0 & 0 & \sigma_h^2 \end{bmatrix} \tag{4}$$

When required by air traffic management, aircraft with advanced equipment (e.g., a flight management system) can control their times of arrival at waypoints along its track. It has been applied widely in the current National Airspace System (NAS) for air traffic controllers to more precisely control aircraft trajectories, especially in congested airspace. As discussed in Hwang's work [18], the tolerance of these controlled times of arrival can then be used to define the growth rate σ_a.

Once the error covariance Σ is decided, the covariance in the Earth frame Σ_e can then be obtained by a simple rotation to align with the heading of the nominal trajectory:

$$\Sigma_e = R_e^h \Sigma R_e^{hT} \tag{5}$$

Figure 1 shows two sample operational intents for Global Hawk operations. Figure 1(a) depicts the operational intent with a short time horizon (about 45 minutes) with a three-minute interval. And Figure 1(b) presents the operational intent with a long time horizon (over three hours) with a ten-minute interval. In both cases, aircraft fly at a constant true airspeed of 340 knots. The wind is predicted to be 15 knots from the southwest. The root mean square deviation of wind prediction errors is assumed 5 knots, and the rms of cross-track errors in navigation, tracking, and control is assumed to be one nautical mile. The dashed line represents the estimated nominal trajectory, and the ellipses are the lateral boundaries of the probabilistic locations for the aircraft at the 3σ confidence level. It is noted that the along-track error grows with time at the rate of 5 knots due to the wind prediction error, whereas the cross-track error remains constant. While the plot shows the instantaneous operational intent for the aircraft at a given time, polygons with combined ellipses can be used to show probabilistic locations for a given time period, although the distribution within the polygons won't be a pure normal distribution.

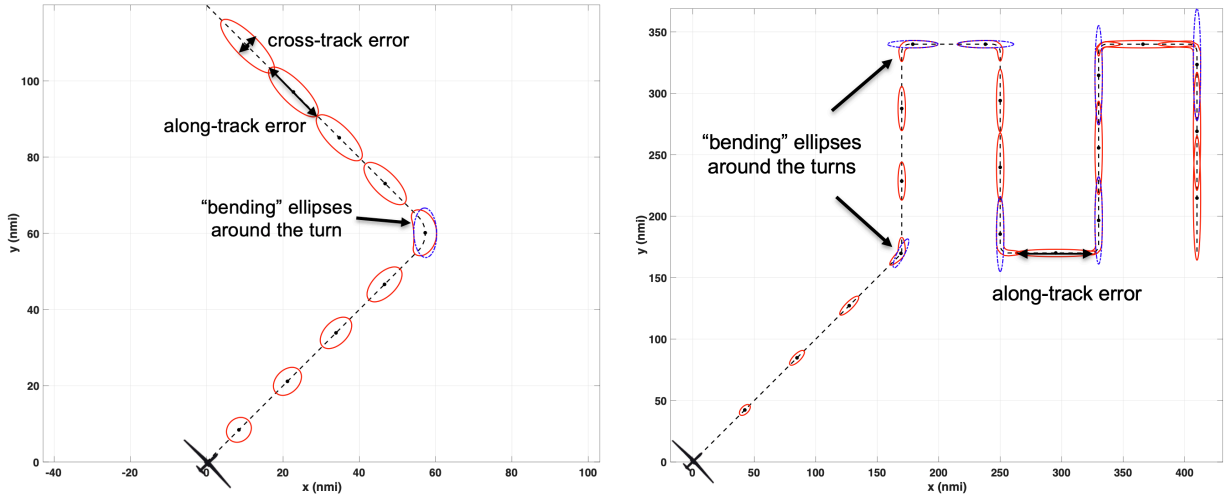

(a) Operational intent with a short time horizon

(b) Operational intent with a long time horizon

Fig. 1 Probabilistic operational intents with adequate lateral control

It's worth mentioning that directly building error ellipses around the nominal trajectory position during turns, like the blue dash-dotted ellipses in the figures, is not correct due to the vehicle's bounded performance in cross-track errors. That inaccuracy gets worse when the look-ahead time is longer, as shown in Figure 1(b). These error ellipses need to bend to follow the nominal trajectory during the turning segments. This adjustment is not just for plotting, but is also needed for intent conflict probability calculation, which will be covered in the following sections.

B. With inadequate lateral control

For vehicles that have inadequate lateral control, the errors in wind prediction will affect the cross-track error as well. The error covariance then becomes Eqn. 6, where σ_a and σ_c represent the root mean square deviations between the wind speed prediction and the actual wind speed along the track and cross the track, respectively. For a balloon, since it only has control over altitude and does not have any lateral control, its cross-track error will grow with time at

the same rate as the along-track error if the wind prediction errors are uniform in all directions. However, for an airship, the growth rates for cross-track and along-track errors could be different.

$$\Sigma(t_i) = \begin{bmatrix} \sigma_a^2(t_i - t_0)^2 & 0 & 0 \\ 0 & \sigma_c^2(t_i - t_0)^2 & 0 \\ 0 & 0 & \sigma_h^2 \end{bmatrix} \tag{6}$$

Figure 2(a) shows a sample operational intent for a low-speed HALE fixed-wing aircraft (e.g., Aurora) with a 20-minute interval, and Figure 2(b) presents a sample operational intent for a free-floating balloon with a 30-minute interval. Both vehicles fly in a wind field with an average wind speed of 20 knots from the southwest. The root mean square deviations of wind prediction errors are assumed 5 and 2 knots for the HALE fixed-wing and balloon, respectively. The dashed line represents the estimated nominal trajectory of the vehicle.

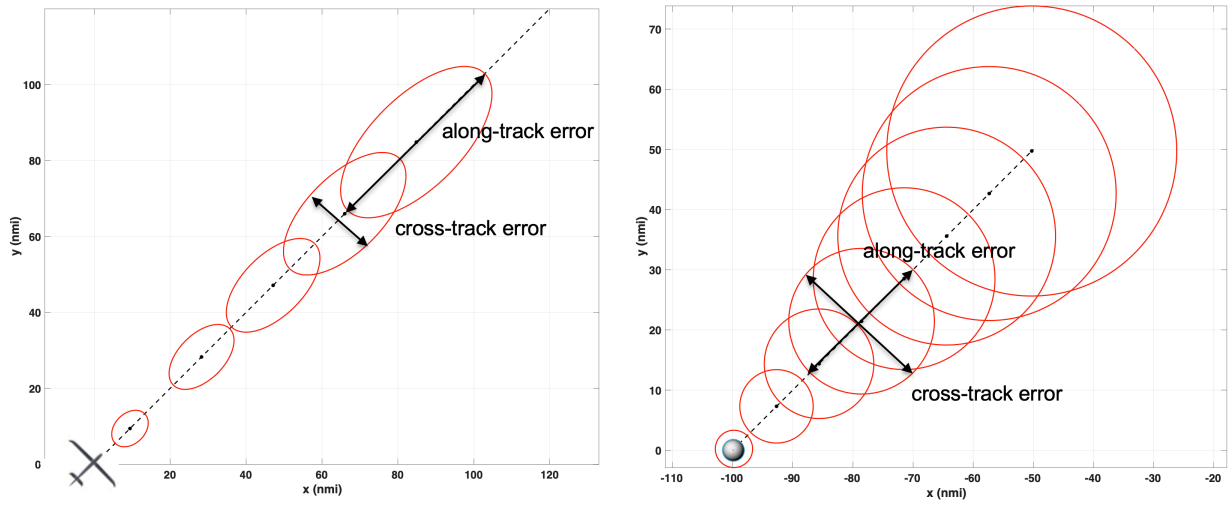

(a) HALE fixed-wing aircraft

(b) Balloon

Fig. 2 Probabilistic operational intents with inadequate lateral control

C. Simulation verification

To verify the probabilistic operational intent model, the Fe^3 fast-time simulator [19] was utilized for Monte Carlo simulations with newly integrated vehicle trajectory models for a balloon and a Global Hawk. The three-dimensional balloon model considers translational dynamics of the balloon with a proportional-integral controller to track the desired altitude. A kinetic point mass model [20, 21] is used with updated Global Hawk parameters [22]. Proportional and proportional-derivative controllers were used to track desired airspeed, horizontal path, and vertical profile.

As discussed in previous sections, when an aerial vehicle flies at a constant true airspeed within certain upper and lower bounds defined by its guidance, navigation, and control performance, the rest of the uncertainty largely comes from wind prediction errors. Every wind prediction model or product has inherent error. As one of the few wind prediction products for the high altitude atmosphere, systematic errors in the Global Forecast System(GFS) [23] were studied by the community [24, 25] as well. Without loss of generality, it is fair to assume the wind prediction errors follow a normal distribution. To feed the random wind errors into the simulator for Monte Carlo simulations, the wind error distributions were assigned to each simulation, as well as, how often the randomness of the wind errors were changed within each simulation.

When constructing the wind prediction errors in simulations, the step duration is used to define how often the random errors change within each simulation. Figures 3(a), 3(b), and 3(c) show the probabilistic positions at different specified times generated by Monte Carlo simulations. A total of 5,000 simulations were conducted for each plot. The predicted wind is 20 knots from the southwest, and the prediction errors are assumed to follow a zero-mean normal

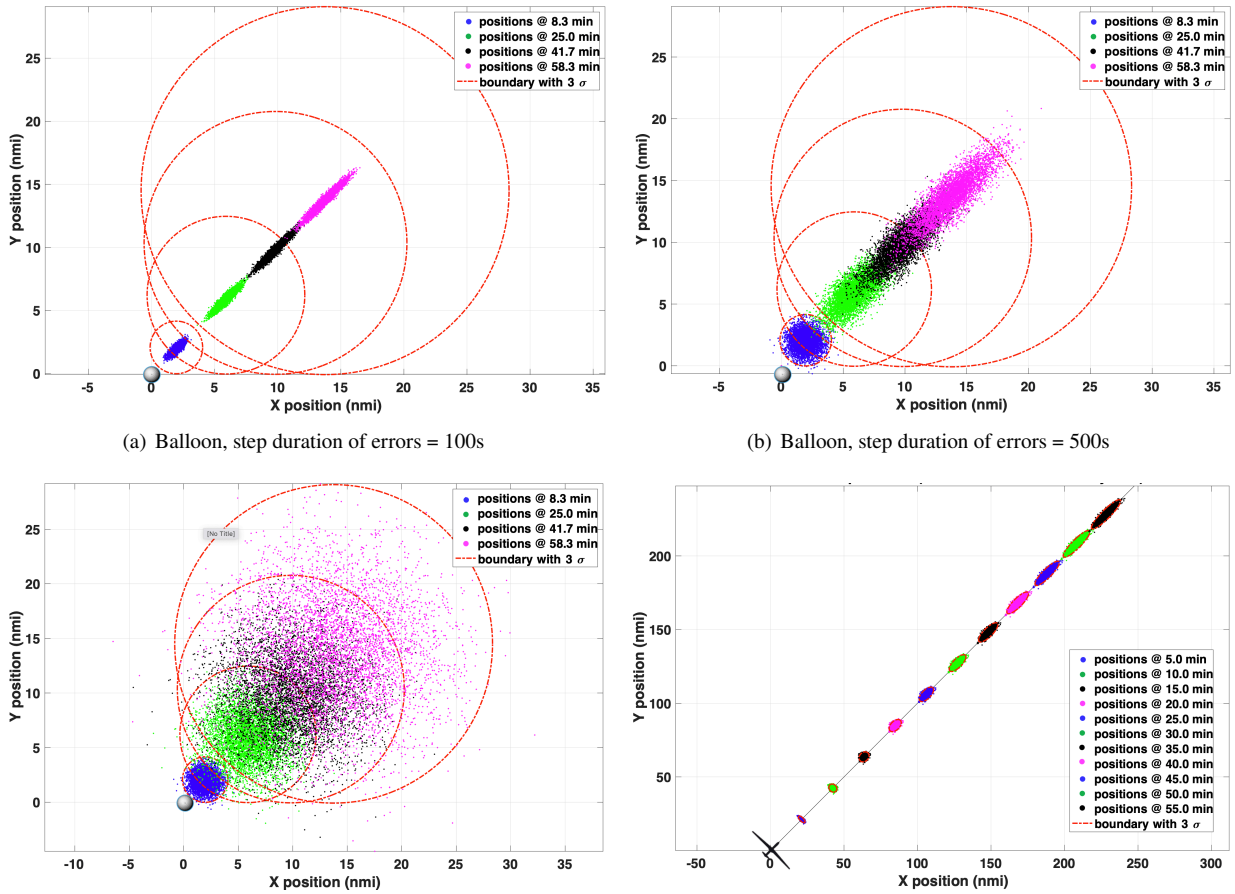

(a) Balloon, step duration of errors = 100s

(b) Balloon, step duration of errors = 500s

(c) Balloon, step duration of errors= ∞ s

(d) Fixed-wing aircraft, step duration of errors = ∞ s

Fig. 3 Probabilistic position prediction using wind errors with varied step duration

distribution with a standard deviation of 7 knots. The 3σ boundaries calculated using Eqn. 6 at corresponding times are presented in red dashed lines as references. Figures 3(a), 3(b), and 3(c) show that, one hour later, the mean location of the balloon is located at around 20 nmi northeast of the starting position. However, the areas of probabilistic locations of the balloon are mainly affected by the step duration of the wind errors. Figures 3(a) and 3(b) show the results when the wind errors were updated every 100 seconds and 500 seconds, respectively, within each simulation. Figures 3(c) and 3(d) depict the results when the wind errors were never updated within each simulation for a balloon and a Global Hawk fixed-wing, respectively. In Figure 3(d), the Global Hawk is assumed to fly at a constant true airspeed. These figures show that future vehicle position uncertainty was less when wind errors were changed more frequently. The fixed random errors in each Monte Carlo simulation provide the most conservative prediction of vehicle position. Figures 3(c) and 3(d) also show that the probabilistic positions match the boundaries calculated by Eqn. 6 quite well.

III. Methods to Calculate Intent Conflict Probability

The main purpose of formulating operational intent is to facilitate the calculation of intent conflict probability and support strategic planning for upper class E airspace operations. There have been many studies [17, 18] on conflict probability calculation for probabilistic positions following normal distributions. Although, these works largely focused on calculating tactical conflict probability, with a certain extension, they can be leveraged for strategic conflict probability calculations as well. This section proposes a hybrid method based on past research and compares the performance and results from these different methods.

A. Paielli and Hwang's methods

Assuming the distribution of vehicle position errors follow a zero mean normal distribution as in Eqn. 3, the probability of the relative distance (λ) between two vehicles at a given time t_i is then:

$$p[\lambda(t_i)] = \mathcal{N}(\lambda(t_i); \bar{\lambda}(t_i), \Sigma_{12}(t_i)) \tag{7}$$

where

$$\bar{\lambda}(t_i) = \|\bar{\vec{x}}_1(t_i) - \bar{\vec{x}}_2(t_i)\| \tag{8}$$

$$\Sigma_{12}(t_i) = \Sigma_1(t_i) + \Sigma_2(t_i) \tag{9}$$

Here $\bar{\vec{x}}_1(t_i)$ and $\bar{\vec{x}}_2(t_i)$ represent the mean positions of two vehicles, respectively, and $\bar{\lambda}$ denotes the mean relative distance.

The intent conflict probability at any time t_i can then be expressed as Eqn. 10, which is computing the probability when the distance between two aircraft is less than the predefined minimum separation S_{min}.

$$P = \int_{\lambda < S_{min}} \mathcal{N}(\lambda; \bar{\lambda}, \Sigma_{12})\, d\lambda \tag{10}$$

Because there is no analytical solution for the exact integral in Eqn. 10, two analytical methods have been developed by Paielli [17] and Hwang [18] to approximate the integral. After combining position errors of two vehicles as in Eqn. 8 (notionally shown as the error ellipse in Fig. 4(a) as well), in both methods, the combined error ellipse and the separation circle are then transformed to make the combined error ellipse a unit circle as shown in Fig. 4(b). The conflict probability is then essentially the integral of probability over the overlapped area between the circle and ellipse. From there, Paielli assumes a constant relative velocity vector and calculates the overlap between the unit circle and the extended conflict zone with an infinite length. While Paielli's method proposed an innovative way to approximate the integral for the conflict probability analytically, the drawback of integrating over the extended zone is that this method will not be accurate, or even correct, when the relative velocity is not constant, especially when one or both vehicles are turning. As shown in Fig. 4(c), Paielli's method will yield a high conflict probability even if one aircraft plans a left turn far before a potential conflict could happen. Hwang's work [18] greatly improves the approximation by integrating over the rectangle enclosing the ellipse (shown as the dashed blue rectangle in Fig. 4(d)) and computes the probability over the overlapped area between the unit circle and the newly-formed rectangle.*

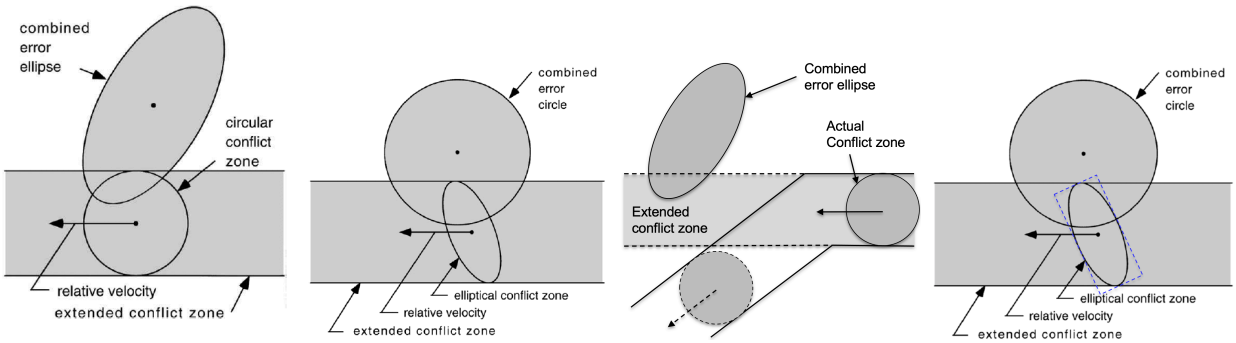

(a) Combine error ellipse and circular conflict zone [17]

(b) transformed combined error circle and elliptical conflict zone [17]

(c) Drawback of using extended conflict zone

(d) Approximate the instantaneous probability using a rectangular [17, 18]

Fig. 4 Calculation of the probability of intent conflict

B. Hybrid method

Both Paielli and Hwang's methods developed a closed-form approximation to the integral of two normal distributions when two aircraft are within a given distance range, and Hwang's method provides improved approximation when

*The final proposed method in [18] used an even granular approximation by cutting corners of the rectangular box outside the ellipse.

compared with Paielli's method. However, both approximation methods assume regular normal distributions for the probabilistic position (e.g., straight error ellipses) at every waypoint along the nominal trajectory. As discussed in the previous section, the normal distribution around the turns should follow the nominal trajectory (like those "bending" error ellipses shown in Figure 1) because of the vehicle's controllability in cross-track errors. Using a regular error ellipse will not be correct, especially when the look-ahead time is long and the along-track error grows a lot, as shown in Figure 1(b). Because strategic management will play a paramount role in upper class E airspace management, to handle intent conflict probability with a long time horizon, a numerical method is needed to calculate the probability around turns. To correctly compute the conflict probability, a hybrid method that uses different methods to compute the conflict probability in different situations is proposed.

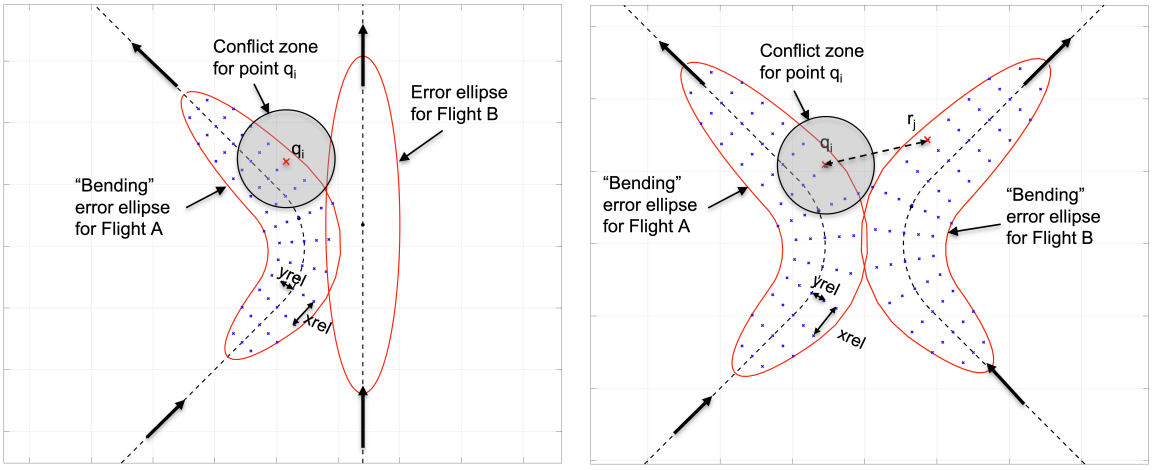

(a) Case I: only one has the "bending" error ellipse

(b) Case II: both flights have "bending" error ellipses

Fig. 5 Numerical calculation of intent conflict probability around a turn

Figure 5 demonstrates two possible cases when calculating intent conflict probability around a turn, where both Flight A and B fly in the directions following the arrows. Figure 5(a) depicts a case when one flight is at a turn, and the other flight is flying straight forward. The error ellipses show the 3σ boundaries at the same time. The error ellipse for Flight A is bending because the turn will be bounded by the cross-track performance of Flight A. To numerically calculate the conflict probability, sample points with the specified resolution "$xrel$" and "$yrel$" are selected within the "bending" error ellipse. In this figure, both are set to 1 nmi. Each point will then be assigned a weight c_i proportional to its frequency in the normal distribution. As shown in the figure, at each point "q_i", there will be a circular conflict zone. The instantaneous conflict probability P between Flight A and Flight B will be:

$$P = \sum_{i=1}^{N} c_i \cdot P_{q_i} \tag{11}$$

where the conflict probability, P_{q_i}, between the point "q_i" and the error ellipse of Flight B can be computed using Hwang's approximation method with the covariance Σ_B from Flight B and the relative distance λ between Point "q_i" and the mean position of Flight B, $\bar{\vec{x}}_B$, as shown in Eqns. 12 and 13:

$$P_{q_i} = \int_{\lambda < S_{min}} \mathcal{N}(\lambda; \bar{\lambda}, \Sigma_B)\, d\lambda \tag{12}$$

$$\bar{\lambda} = \|\bar{\vec{q}}_i - \bar{\vec{x}}_B\| \tag{13}$$

Figure 5(b) presents another case when both flights are at their turns. To compute the intent conflict probability, sample points need to be taken within both bending error ellipses. Each sample point will be assigned with a weight proportional to its frequency in the normal distribution. c_i and k_j are the weights for points q_i and r_j associated with

Flight A and B, respectively. The instantaneous conflict probability can still use Eqn. 11, however, the way of calculating the conflict probability at Point q_i becomes:

$$P_{q_i} = \sum_{j=1}^{M} k_j \cdot (\|\vec{q}_i - \vec{r}_j\| < S_{min}) \tag{14}$$

With N sample points from Flight A and M points from Flight B, the relative distance check needs to be done $M \times N$ times.

C. Comparison: computational time and accuracy

The proposed hybrid method uses three methods to compute three types of scenarios, respectively. Scenario I is when two flights are within their straight segments; Scenario II is when one flight is at its turning segment; and Scenario III is when both flights are at their turning segments. Table 1 summarizes the computation methods and their computational times. The computational times were measured by running the Matlab script on a MacBook Pro with 2.6 GHz 6-Core Intel Core i7 and 16 GB 2667 MHz DDR4 memory. Note that computational times for Scenario II and III are proportional to the total number of sample points selected. In this table, the number of sample points in Scenario II N is 63. Since in Scenario II, the conflict probability of each point is calculated the same as in Scenario I, the resulting computational time is about 60 times that of Scenario I. Although the number of sample points in Scenario III is $M \times N = 60 \times 63$, since the distance-checking between each pair of points is less time-consuming compared to the matrix manipulation in Scenario I, the total time is only about 30 times that of Scenario I. The computational effort shows that the proposed hybrid method should be able to compute and update the intent conflict probabilities between two flights within a certain time horizon in real-time.

Table 1 Comparison of computational times

Types of scenarios	Scenario I: Two regular error ellipses	Scenario II: One "bending" and one regular error ellipses	Scenario III: Two "bending" error ellipses
Calculating method	Eqns. 7, 8, 9, and 10	Eqns. 11, 12, and 13	Eqns. 11 and 14
Computational time	0.098 ms	6.0 ms	2.96 ms

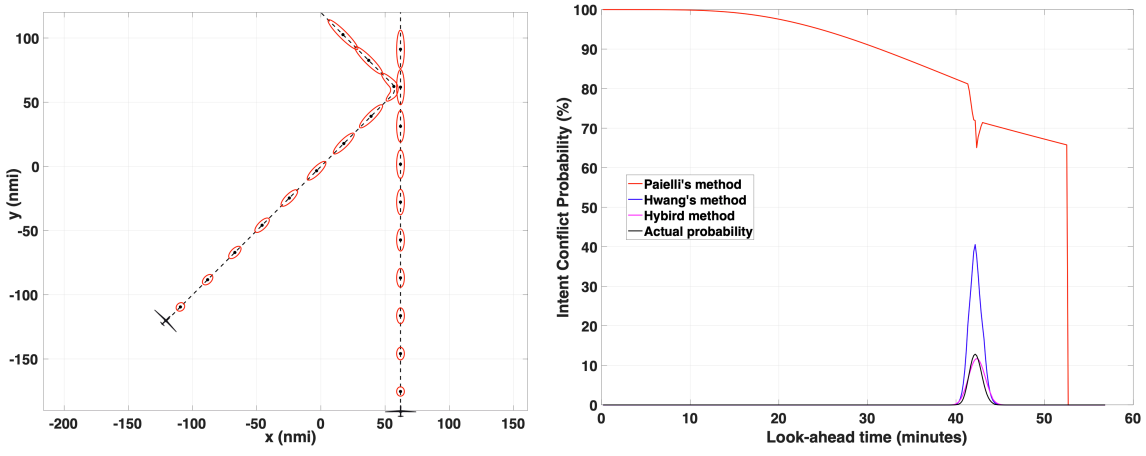

(a) Flight operational intent and nominal trajectories

(b) Intent conflict probability using different methods

Fig. 6 Comparison of different methods for intent conflict probability

To compare the probability calculated by different methods, Figure 6(a) depicts a scenario where one flight is

planning to fly northeast and then make a left turn before crossing another flight's path, while another flight is planning to simply fly north. The ellipses shown in the figure are the boundaries with the confidence level of 3σ for each aircraft's probabilistic positions. For better visualization, these boundaries are shown at a fixed interval. Figure 6(b) presents the probabilities computed by three methods and the actual probability based on simulated trajectories. These probabilities cover the period from the current time to 50 minutes ahead. The red curve is the probabilities computed by Paielli's method; the blue curve represents the results based on Hwang's method; the magenta curve is calculated using the hybrid method proposed in this work; and the black curve is the actual probabilities.

It is noticed that Paielli's method did not consider the turn when calculating the conflict probability for the first segments (< 40 minutes). The probability decreased for the first segment because of the increased uncertainties. A similar situation happened for the segment after the turn as well. Hwang's method improved the probability calculation through a refined approximation, and the results reflected the intent conflict probability more accurately. In this case, the conflict probability is close to zero during the straight segments and nonzero during the turn. However, since Hwang's method did not consider the bending normal distribution resulting from the aircraft's cross-track performance during the turn, its probability calculation is not accurate at the turn. The peak conflict probability during the turn is about 40%. The hybrid method computes the conflict probability during the turn differently. The results showed that the peak probability during the turn is about 10%, which matches the actual probability quite well.

IV. Illustrative Example of Strategic Planning

Using the proposed hybrid method and the operational intent model developed upon the knowledge of flight plan, vehicle flight performance, and wind prediction errors, the intent conflict probability can be calculated to facilitate strategic planning. This section presents an example for illustration [†].

Assuming there is a balloon operating above a mountainous area at 60,000 ft MSL in California to provide communication services, a Global Hawk is planned to fly to the same area for wildfire monitoring at the same altitude. The wind is predicted to be 20 knots from the southwest, and the rms of the prediction error is 5 knots.

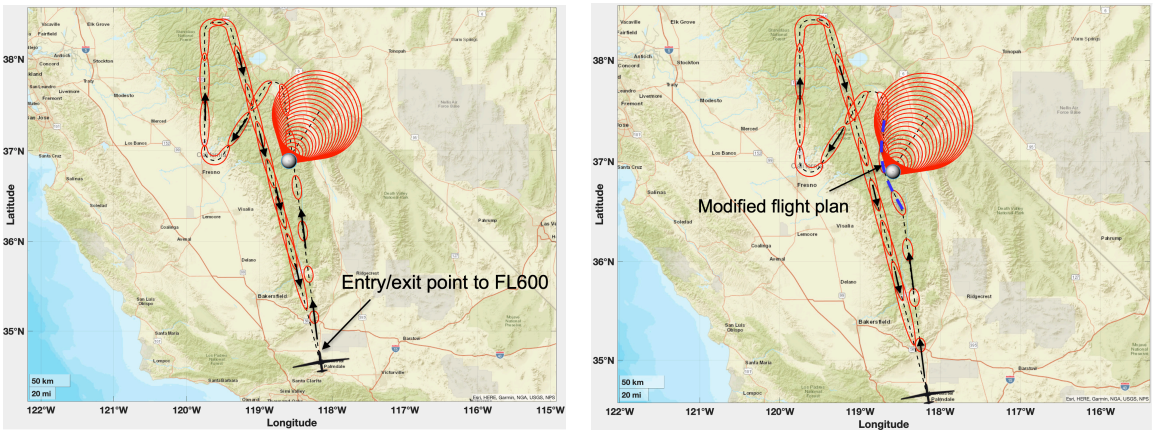

(a) Original operational intents

(b) Operational intents with modified flight plan

Fig. 7 Example of intent conflict probability in strategic planning

According to flight plans, performances, and the wind prediction information, their operational intents are generated using the method proposed in Section II. The operational intents with certain intervals are shown in Figure 7(a). Applying the hybrid method proposed in Section III.B, the time history of the intent conflict probability over different look-ahead time horizons is shown as the red curve in Figure 8 with a peak intent conflict probability of 75% around 22 minutes from when the Global Hawk reaches FL600. If the Global Hawk operator wants to reduce the intent conflict likelihood to less than 5% during the strategic planning stage, two possible options are shown here: delaying the time to the entry point by 60 minutes; or modifying the flight plan path by adding a detour waypoint as shown in Figure 7(b). Both options will then lower the conflict probability to less than 5% as shown in Figure 8.

[†]The example is not created based on historic operations

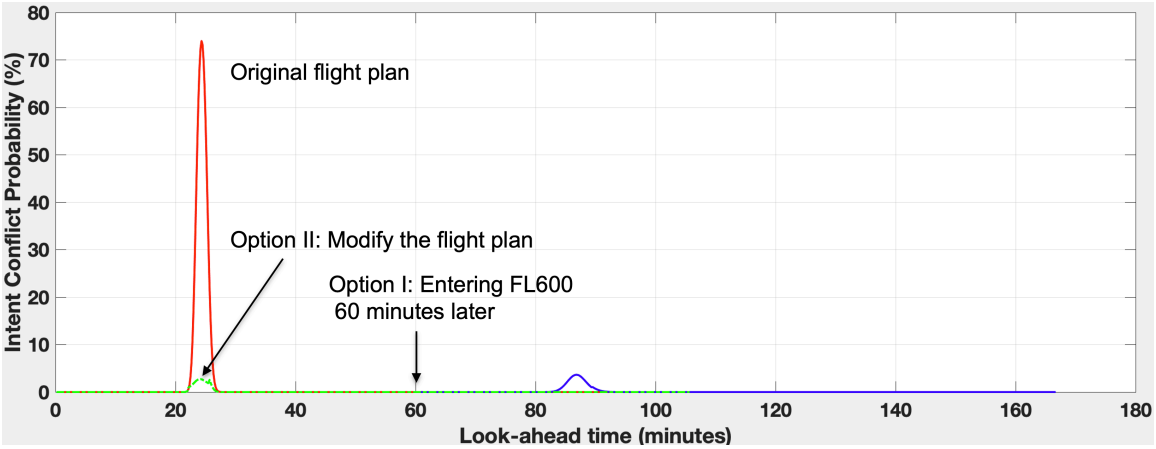

Fig. 8 Reducing the operational intent conflict probability through strategic planning

This example showed a snapshot of the strategic planning process. Since the operational intent can be updated while the aircraft or balloon is flying or when the wind prediction is refreshed, the corresponding intent conflict probability can be constantly recalculated to reflect the updated situation and assist any further decision-making for strategic planning.

V. Conclusions

High altitude operations above FL600 allow broader and more persistent service area coverage than at ground level and has attracted the development of many commercial applications. Balloons, airships, high-altitude long-endurance (HALE) aerial vehicles, and supersonic aircraft have been developed to provide platforms to enable these high-altitude operations. As the foundation for the operator to share their intents, the operational intent model plays a critical role in safe, efficient, fair, and scalable operations. The intent model and sharing of this information is also a key to integrating various vehicle types and operations.

This work first proposed a probabilistic intent model for the variety of vehicles in an ETM environment. Simulation results verified that the probabilistic intent model reflects the uncertain positions resulting from vehicle performance and wind prediction errors. Furthermore, a hybrid method is developed to calculate the intent conflict probability by extending past works on probabilistic conflict computation. The comparison with past methods showed that the proposed hybrid method computes the intent conflict probability with greater accuracy around turns, especially for a long look-ahead horizon. Furthermore, the computational time of the proposed hybrid method is suitable for real-time applications. An example was presented to illustrate the usage of the intent conflict probability for strategic planning.

References

[1] Bellemare, M. G., Candido, S., Castro, P. S., Gong, J., Machado, M. C., Moitra, S., Ponda, S. S., and Wang, Z., "Autonomous Navigation of Stratospheric Balloons using Reinforcement Learning," *Nature*, Vol. 588, 2020, pp. 77–88.

[2] "Sceye Inc. to Build Stratospheric Airships in NM," *Albuquerque Journal*, 2020. URL `https://www.abqjournal.com/1487318/sceye-inc-to-build-stratospheric-airships-in-nm.html`.

[3] "HAPSMobile's Sunglider Succeeds in Stratospheric Test Flight," *sUAS News*, 2020. URL `https://www.suasnews.com/2020/10/hapsmobiles-sunglider-succeeds-in-stratospheric-test-flight/`.

[4] Martin, R. A., Gates, N. S., Ning, A., and Hedengren, J. D., "Dynamic Optimization of High-altitude Solar Aircraft Trajectories Under Station-Keeping Constraints," *AIAA Journal of Guidance, Control, and Dynamics*, Vol. 42, No. 3, 2019, pp. 538–552.

[5] *Upper Class E Traffic Management (ETM) Concept of Operations*, FAA, 2020. URL `https://www.faa.gov/uas/advanced_operations/upper_class_etm/`.

[6] Wang, C., Baets, P., Fenkell, M., Tailby, A., Barry, S., Taylor, P., Bouygues, L., Mian, Z., Gentry, J., and Kluttz, B., "Adaptive Risk-based Conflict Detection for Stratospheric Flight Operations," *Air Traffic Control Association Tech Symposium*, Virtual, 2020.

[7] Jung, J., Rios, J., Xue, M., Homola, J., and Lee, P., "Overview of NASA's Extensible Traffic Management (xTM) Work," *AIAA Scitech Conferencet*, San Diego, CA, 2022.

[8] Yoo, H., Li, J., Homola, J., and Jung, J., "Cooperative Upper Class E Airspace: Concept of Operations and Simulation Development for Operational Feasibility Assessment," *AIAA Aviation 2021*, Virtual, 2021.

[9] *NASA Unmanned Aircraft Systems (UAS) Traffic Management (UTM) Project*, NASA, 2020. URL `https://www.nasa.gov/utm/`.

[10] RTCA, "Free Flight Implementation," *Final Report of ETCA Task Force*, Washington D.C., 1995.

[11] Zhao, Y., Haissig, C., and Hoffman, M. J., "Analysis of Pilot Intent Parameters in Air Traffic Management," *Proceedings of the American Control Conference*, Philadelphia, PA, 1998.

[12] Ruigrok, R., and Valent Clari, M., "The Impact Of Aircraft Intent Information And Traffic Separation Assurance Responsibility on En-route Airspace Capacity," *2003 ATM R&D Seminar*, Budapest, Hungary, 2003.

[13] Mueller, K., and Krozel, J., "Aircraft ADS-B intent verification based on a Kalman tracking filter," *AIAA Guidance, Navigation, and Control Conference and Exhibit*, Denver, CO, 2000. doi:10.2514/6.2000-4067.

[14] Krozel, J., and Andrisani, D., "Intent Inference and Strategic Path Prediction," *AIAA Guidance, Navigation, and Control Conference and Exhibit*, San Francisco, CA, 2005.

[15] Yang, L. C., and Kuchar, J. K., "Using Intent Information In Probabilistic Conflict Analysis," *AIAA Guidance, Navigation, and Control*, Boston, MA, 1998.

[16] *UTM Concept of Operations v2.0*, FAA, 2020. URL `https://www.faa.gov/uas/research_development/traffic_management/media/UTM_ConOps_v2.pdf`.

[17] Paielli, R. A., and Erzberger, H., "Conflict Probability Estimation for Free Flight," *AIAA Journal of Guidance, Control, and Dynamics*, Vol. 20, No. 3, 1997, pp. 588–596.

[18] Hwang, I., and Seah, C. E., "Intent-Based Probabilistic Conflict Detection for the Next Generation Air Transportation System," *Proceedings of the IEEE*, Vol. 96, No. 12, 2008, pp. 2040–2059. doi:10.1109/JPROC.2008.2006138.

[19] Xue, M., Rios, J., Silva, J., Ishihara, A., and Zhu, Z., "Fe^3: An Evaluation Tool for Low-Altitude Air Traffic Operations," *AIAA Aviation Forum*, Atlanta, GA, 2018.

[20] Chatterji, G. B., Sridhar, B., and Bilimoria, K. D., "En-route Flight Trajectory Prediction for Conflict Avoidance and Traffic Management," *AIAA Guidance, Navigation, and Control Conference*, San Diego, CA, 1996.

[21] Chatterji, G. B., "Trajectory Simulation for Air Traffic Management Employing a Multirotor Urban Air Mobility Aircraft Model," *AIAA Aviation*, Virtual event, 2020.

[22] Pastor, E., Perez-Batlle, M., Barrado, C., Royo, P., and Cuadrado, R., "A Macroscopic Performance Analysis of NASA's Northrop Grumman RQ-4A," *Aerospace*, Vol. 5, No. 1, 2018, pp. 1–16.

[23] *Global Forecast System0*, NOAA, ???? URL `https://www.ncei.noaa.gov/products/weather-climate-models/global-forecast`.

[24] Danforth, C. M., Kalnay, E., and Miyoshi, T., "Estimating and correcting global weather model error," *Monthly Weather Review*, Vol. 135, 2007, pp. 281–299.

[25] Bhargava, K., Kalnay, E., Carton, J. A., and Yang, F., "Estimation of Systematic Errors in the GFS Using Analysis Increments," *Journal of Geophysical Research: Atmospheres*, Vol. 123, 2018, pp. 1626–1637.